NeuroImage 184 (2019) 717–728

Contents lists available at ScienceDirect

NeuroImage

journal homepage: www.elsevier.com/locate/neuroimage

Dual-calibrated fMRI measurement of absolute cerebral metabolic rate of oxygen consumption and effective oxygen diffusivity

M. Germuska [a], H.L. Chandler [a], R.C. Stickland [a], C. Foster [a], F. Fasano [b], T.W. Okell [d], J. Steventon [a], V. Tomassini [c,a], K. Murphy [a], R.G. Wise [a,*]

[a] Cardiff University Brain Research Imaging Centre, School of Psychology, Cardiff University, Cardiff, UK
[b] Siemens Healthcare Ltd, Frimley, Camberley, UK
[c] Division of Psychological Medicine and Clinical Neurosciences, Cardiff University School of Medicine, Cardiff, UK
[d] Wellcome Centre for Integrative Neuroimaging, FMRIB, Nuffield Department of Clinical Neurosciences, University of Oxford, UK

A B S T R A C T

Dual-calibrated fMRI is a multi-parametric technique that allows for the quantification of the resting oxygen extraction fraction (OEF), the absolute rate of cerebral metabolic oxygen consumption ($CMRO_2$), cerebral vascular reactivity (CVR) and baseline perfusion (CBF). It combines measurements of arterial spin labelling (ASL) and blood oxygenation level dependent (BOLD) signal changes during hypercapnic and hyperoxic gas challenges. Here we propose an extension to this methodology that permits the simultaneous quantification of the effective oxygen diffusivity of the capillary network (D_C). The effective oxygen diffusivity has the scope to be an informative biomarker and useful adjunct to $CMRO_2$, potentially providing a non-invasive metric of microvascular health, which is known to be disturbed in a range of neurological diseases. We demonstrate the new method in a cohort of healthy volunteers ($n = 19$) both at rest and during visual stimulation. The effective oxygen diffusivity was found to be highly correlated with $CMRO_2$ during rest and activation, consistent with previous PET observations of a strong correlation between metabolic oxygen demand and effective diffusivity. The increase in effective diffusivity during functional activation was found to be consistent with previously reported increases in capillary blood volume, supporting the notion that measured oxygen diffusivity is sensitive to microvascular physiology.

1. Introduction

Calibrated fMRI measurement of absolute cerebral rate of oxygen metabolism ($CMRO_2$) offers a non-invasive method of mapping oxygen consumption in the brain (Bulte et al., 2012; Gauthier et al., 2012; Wise et al., 2013), providing quantitative estimates of a critical physiological function. However, the method does not directly consider the transport of oxygen into the tissue, which is principally constrained by cerebral blood flow (CBF) and the effective oxygen diffusivity of the capillaries (Buxton and Frank, 1997; Gjedde et al., 1999; Hayashi et al., 2003; Hyder et al., 1998; Mintun et al., 2001; Vafaee and Gjedde, 2000; Valabregue et al., 2003; Zheng et al., 2002). Effective oxygen diffusivity summarises the practical ability of the capillary network for oxygen diffusion into the tissue and limits the speed of oxygen transport out of the microvasculature. One of the primary determinants of the effective oxygen diffusivity is the capillary density (Gjedde et al., 1999), which is known to be associated with mitochondrial density (Hoppeler and Kayar, 1988) and metabolic demand (Harrison et al., 2002). Thus, brain regions with a high resting $CMRO_2$ are found to be co-localised with regions of high capillary density (Sette et al., 1989). However, the effective diffusivity does not appear to be a fixed property of the tissue and may play a crucial role in neurovascular coupling, with oxygen diffusivity being observed to parallel increases in demand and compensate for reductions in oxygen delivery (Hayashi et al., 2003, 2004; Hyder et al., 1998; Vafaee and Gjedde, 2000).

Compartmental models of oxygen exchange between the capillaries and tissue offer a means of estimating the effective oxygen diffusivity from observations of blood flow and oxygen extraction. The model proposed by (Hyder et al., 1998) suggests a need for the effective diffusivity to increase during functional hyperaemia in order to meet the metabolic demands of neural activation. Based on a meta-analysis of CBF and $CMRO_2$ measurements from a variety of modalities Hyder et al. proposed a linear coupling between flow and effective diffusivity to account for this apparently coupled behaviour. Evidence for this linear relationship between the effective oxygen diffusivity and CBF was demonstrated with a combined MRI and MRS approach in rat (Hyder et al., 2000). However, PET experiments conducted by (Vafaee and Gjedde, 2000) demonstrate a need for the oxygen diffusivity to adapt to the current metabolic demand,

* Corresponding author.
E-mail address: wiserg@cardiff.ac.uk (R.G. Wise).

https://doi.org/10.1016/j.neuroimage.2018.09.035
Received 14 March 2018; Received in revised form 11 September 2018; Accepted 14 September 2018
Available online 29 September 2018

with alterations in the effective diffusivity appearing to be made independently from cerebral blood flow. Alternatively, more recent analysis presented by (Buxton, 2010) demonstrates that metabolic oxygen demand could be met if there was fixed but significant oxygen tissue content, without the need for adjustment to the oxygen diffusivity. The exact mechanism responsible for any such adaptation to metabolic demand is unclear. However, a plausible candidate for the modulation of the effective diffusivity is via pericyte control of capillary dilation, either through a direct increase in the capillary blood volume, or via a homogenisation of flow heterogeneity (Jespersen and Ostergaard, 2012). Thus, measurement of the effective diffusivity may in fact provide a non-invasive probe to investigate the health and action of capillary pericytes, whose function is known to be degraded in multiple neurodegenerative diseases and stroke (Winkler et al., 2013; Yemisci et al., 2009; Zlokovic, 2011).

In the work presented here we use a compartmental model of oxygen exchange to model the relationship between blood flow, effective diffusivity and oxygen extraction. The model is included within a dual-calibrated fMRI estimation framework (Germuska et al., 2016) to enable simultaneous estimates of the resting blood flow, oxygen extraction fraction (OEF), effective diffusivity, and $CMRO_2$. The aim of this study was to examine the coupling between consumption ($CMRO_2$) and diffusivity at rest, and in response to neural activation (a visual checkerboard task) using the newly proposed method. Our first hypothesis was that, due to the tight functional-structural coupling between capillary density and resting metabolism, there would be a strong correlation between the basal $CMRO_2$ and effective diffusivity. Secondly, we hypothesised that the increased metabolic demand due to the visual task would result in a parallel increase in effective diffusivity, whose magnitude should be consistent with published recordings of functional capillary recruitment (Hall et al., 2014).

2. Methods

2.1. Compartmental modelling

The compartmental model of oxygen exchange is based on the model of (Hayashi et al., 2003). As shown in Fig. 1, the model contains a single capillary compartment with area A and length L, which exchanges oxygen with a cylindrical volume of tissue. The capillary has two compartments, a haemoglobin compartment (with oxygen content C_B) and a plasma compartment (with oxygen partial pressure P). The oxygen in plasma is assumed to be in equilibrium with the oxygen bound to haemoglobin as described by the Hill equation below

$$P = P_{50} \cdot (C_B/(\varphi \cdot [Hb] - C_B))^{1/h} \quad (1)$$

where P is the partial pressure of oxygen in the plasma, P_{50} is the oxygen partial pressure at half saturation, [Hb] is the haemoglobin concentration (g/ml), φ is the oxygen binding capacity for Hb (1.34 ml/g), h is the Hill coefficient (2.8), and C_B (oxygen bound to haemoglobin) is equal to total capillary oxygen content, C_t, if the contribution of plasma oxygen is neglected.

As blood travels along the capillary, the oxygen exchanges between an infinitesimally thin element of blood plasma and a well-stirred oxygen compartment some fixed distance from the capillary (with partial pressure P_m). The permeability of the capillary endothelium and brain tissue are combined into a single effective permeability, k. This interpretation of the model is a departure from the model presented by (Hayashi et al., 2003), who assumed a uniform partial pressure of oxygen in the radial slice of plasma and zero partial pressure of oxygen on the tissue side of the capillary-tissue interface, thus, localising the oxygen transport to within the capillary endothelium. However, *in-vivo* measurements suggest that the capillary wall does not present a significant barrier to oxygen diffusion (Duling et al., 1979), which is instead provided by the tissue (Hudetz, 1999). Thus, as per (Hyder et al., 1998), we combine both the capillary wall and the surrounding brain tissue into a single interface between the plasma and a well-stirred pool at the end of the diffusion path, which is presumably within or surrounding the mitochondria.

From our compartmental model we can define the differential equation describing the loss of oxygen from within a capillary as

$$\frac{dC_t(x,t)}{dt} = -k(P(x,t) - P_m(t)) \quad (2)$$

where t is time, x is the fractional distance along the capillary (0,1), k is the effective permeability (mL/mmHg/mL/min), P is the oxygen partial pressure in the plasma (mmHg), and P_m is the oxygen partial pressure at the mitochondria (mmHg).

Following (Zheng et al., 2002) and (Hayashi et al., 2003)

$$CBF = A \cdot L \cdot \frac{dx}{dt} = V \cdot \frac{dx}{dt} \quad (3)$$

and when blood flow is constant

$$\frac{dC_t}{dt} = \frac{dC_t}{dx} \cdot \frac{dx}{dt} \quad (4)$$

where CBF is cerebral blood flow in ml/100 g/min, A is the cross-sectional area of the capillary, L is the length, and V is the volume in ml/100g. Thus, by substituting equations (3) and (4) into equation (2) we obtain

$$\frac{dC_t}{dx} = -\frac{k \cdot V}{CBF}(P - P_m) \quad (5)$$

If we assume that there is minimal partial pressure of oxygen at the mitochondria (Gjedde et al., 1999, 2005; Herman et al., 2006), i.e. $P_m \approx 0$, then the product $k \times V$ is the effective oxygen diffusivity, D_C (ml/100g/mmHg/min). By substituting equation (1) into equation (5), we can express the differential equation of oxygen loss in terms of capillary oxygen content, resting CBF, and the effective oxygen diffusivity as

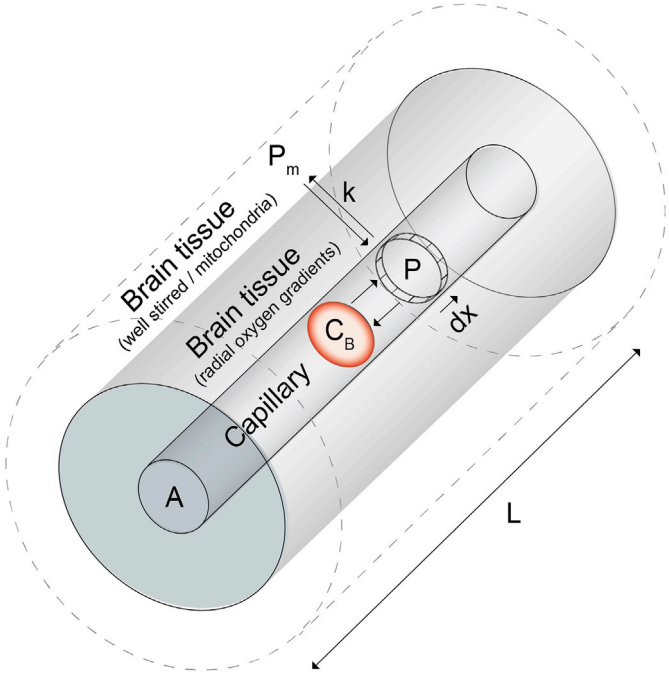

Fig. 1. Schematic of the simple compartmental model for oxygen exchange between capillary blood and brain tissue.

$$\frac{dC_t}{dx} = -\frac{D_c \cdot P_{50}}{CBF} \cdot \left(\frac{C_t}{\varphi \cdot [Hb] - C_t}\right)^{1/h} \quad (6)$$

which is the equivalent to equation (6) in (Hayashi et al., 2003), except that we are assuming negligible oxygen tension at the mitochondria rather than zero average oxygen tension in the tissue.

At the macroscopic level we consider a volume of tissue to contain a collection of identical capillaries arranged such that P_m can be considered uniform (note this does not pre-suppose any particular structural configuration). For simplicity we also assume that all other parameters are identical across the capillaries, such that there is no flow heterogeneity or variation in haemoglobin concentration [Hb]. Thus, the modelled oxygen diffusivity represents a combination of vascular parameters including capillary blood volume, flow heterogeneity, and any underlying variation in P_m.

Equation (6) was solved numerically (using MATLAB's ordinary differential equation solver (Mathworks, MA, USA.)) for different combinations of D_c, CBF, P_{50}, and [Hb] to create a lookup table of results that could be used to fit *in-vivo* data. The oxygen extraction fraction was calculated by evaluating $(C_t(x)|_{x=0} - C_t(x)|_{x=1})/C_t(x)|_{x=0}$ for each combination of parameters, where $C_t(x)|_{x=0}$ is the oxygen content at the arterial end of the capillary (CaO_2), assumed to be 0.95 of the maximum (Jespersen and Ostergaard, 2012), and $C_t(x)|_{x=1}$ is the oxygen content at the venous end of the capillary (CvO_2).

2.2. Calibrated fMRI signal modelling

Quantification of the oxygen extraction fraction and resting blood flow (from which $CMRO_2$ is calculated) is performed using the dual-calibrated fMRI method (Bulte et al., 2012; Gauthier et al., 2012; Wise et al., 2013) within a forward modelling framework (Germuska et al., 2016). The method is based upon the isometabolic alteration of flow and venous oxygenation using hypercapnic and hyperoxic respiratory modulations. Here we utilise the simplified calibration model (Merola et al., 2016), where the change in BOLD signal is defined by equation (7).

$$\frac{\Delta S}{S_0} = TE \cdot \kappa \cdot [dHb]_0 \left\{1 - \left(\frac{CBF}{CBF_0}\right)^{\theta} \left(\frac{[dHb]}{[dHb]_0}\right)\right\} \quad (7)$$

where S is the MR signal magnitude, TE is the echo time of the acquisition, κ is a composite calibration parameter that represents the combination of the venous-weighted blood volume and water diffusion effects, [dHb] is the deoxyhaemoglobin concentration and is equal to [Hb]×(1-S_vO_2), θ (assigned a value of 0.06) is an empirical parameter combining contributions from venous blood volume changes during hypercapnic hyperaemia and extra-vascular water diffusion effects around the microvasculature, and the subscript 0 represents the a parameter's baseline value.

The deoxyhaemoglobin ratio is modelled as shown in equation (8) (Wise et al., 2013), and as before, $OEF = (CaO_2 - CvO_2)/CaO_2$.

$$\frac{[dHb]}{[dHb]_0} = \frac{CBF_0}{CBF} - \frac{1}{[dHb]_0}\left\{\frac{1}{\varphi}\left(CaO_2 - \frac{CBF_0}{CBF} CaO_{2|0}\right) + [Hb]\left(\frac{CBF_0}{CBF} - 1\right)\right\} \quad (8)$$

The arterial spin labelling (ASL) sequence used for the calibrated acquisition uses a pCASL labelling scheme with pre-saturation and background suppression (Okell et al., 2013), and a dual-excitation (DEXI) EPI readout (Schmithorst et al., 2014). As such it differs from the dual-echo PASL acquisition previously employed in the forward modelling framework (Germuska et al., 2016), and the methods have been adapted to reflect this. In the current implementation, BOLD contamination is removed from TE_1 via surround subtraction, and ASL contamination is removed from TE_2 via surround averaging. Thus, only the BOLD model (equations (7) and (8) is used to estimate TE_2 data, while TE_1 time courses are estimated according to the simplified pCASL kinetic model (Alsop et al., 2015), equation (9).

$$\Delta S = \frac{2 \cdot \alpha \cdot \alpha_{inv} \cdot CBF \cdot T_{1,blood} \cdot M_0 \cdot \left(1 - e^{-\frac{\tau}{T_{1,blood}}}\right)}{6000 \cdot \lambda \cdot e^{\frac{PLD}{T_{1,blood}}}} \quad (9)$$

where ΔS is the tag/control difference, α is the tagging inversion efficiency (0.85), α_{inv} is a scaling factor to account for the reduction in tagging efficiency due to background suppression (0.88)(Mutsaerts et al., 2014; Shin et al., 2011), $T_{1,blood}$ is the longitudinal relaxation time of arterial blood, M_0 is the equilibrium magnetisation, λ is the brain/blood partition coefficient (0.9), τ is the tagging duration, and PLD is the post labelling delay. See Table 1 for a summary of the parameters used in the modelling of ASL, BOLD and oxygen exchange.

2.3. Data acquisition

Nineteen healthy volunteers (13 males, mean age 31.9 ± 6.5 years) were recruited to the study. Volunteers' tolerance of hypercapnic periods and breathing through a face-mask was tested with a non-MRI session prior to MRI scanning. The study was approved by the local ethics committee. Written informed consent was obtained from each participant. All data were acquired using a Siemens MAGNETOM Prisma (Siemens Healthcare GmbH, Erlangen) 3T clinical scanner with a 32-

Table 1
Abbreviations for variables and techniques used in the modelling and analysis.

Variable/ abbreviation	Expression (units)
OEF	Oxygen Extraction Faction (dimensionless 0–1)
$CMRO_2$	Cerebral Metabolic Rate of Oxygen consumption (μmol/100 g/min)
CBF	Cerebral Blood Flow (ml/100g/mmHg/min)
CVR	Cerebral Vascular Reactivity (% CFB change/mmHg Co_2)
D_c	Effective oxygen diffusivity of the capillary network (ml/100g/mmHg/min)
P	Oxygen tension in capillary plasma(mmHg)
P_{50}	Oxygen tension at which haemoglobin is 50% saturated (mmHg)
P_m	Oxygen tension at the mitochondria (mmHg)
[Hb]	Haemoglobin concentration (g/ml)
C_B	Oxygen content bound to haemoglobin (ml/ml)
C_t	Total capillary oxygen content (ml/ml)
CaO_2	Oxygen content at the arterial end of the capillary network (ml/ml)
CvO_2	Oxygen content at the venous end of the capillary network (ml/ml)
SaO_2	Arterial oxygen saturation (dimensionless 0–1)
SvO_2	Venous oxygen saturation (dimensionless 0–1)
PaO_2	Arterial oxygen tension (mmHg)
$PaCO_2$	Arterial carbon dioxide tension (mmHg)
$P_{ET}O_2$	End-tidal oxygen tension (mmHg)
$P_{ET}.CO_2$	End-tidal carbon dioxide tension (mmHg)
ϕ	Oxygen binding capacity of haemoglobin (1.34 ml/g)
h	Hill coefficient (2.8)
k	Effective permeability of capillary endothelium and brain tissue (ml/mmHg/ml/min)
ε	Oxygen plasma solubility (0.0031 ml/mmHg/dl)
BOLD	Blood oxygenation level dependent MRI signal
ASL	Arterial spin labelling
TE	Echo time of MRI acquisition (ms)
κ	BOLD calibration parameter including venous-weighted blood volume and water diffusion effects
[dHb]	Deoxyhaemoglobin concentration (g/ml)
θ	Effective hypercapnic venous flow-volume coupling constant (0.06)
$T_{1,blood}$	Longitudinal relaxation time of arterial blood (s)
$R_{1,blood}$	Longitudinal relaxation rate of arterial blood (s^{-1})
M0	MRI signal equilibrium magnetisation (dimensionless)
λ	Brain/blood partition coefficient (dimensionless, 0.9)
τ	Arterial spin labelling tagging duration (s)
PLD	Arterial spin labelling post labelling delay (s)

channel receiver head coil (Siemens Healthcare GmbH, Erlangen). During each scanning session an 18-min dual-calibrated fMRI scan was acquired with interleaved periods of hypercapnia, hyperoxia and medical air being delivered to the subjects according to the protocol previously proposed by our lab (Germuska et al., 2016). End-tidal gases, $P_{ET}CO_2$ and $P_{ET}O_2$, were sampled from the volunteer's facemask using a rapidly responding gas analyzer (AEI Technologies, Pittsburgh, PA, USA), see Fig. 2 for a summary of end-tidal recordings and timings of the gas paradigm.

All calibrated fMRI data were acquired using a prototype pCASL acquisition using pre-saturation and background suppression (Okell et al., 2013) and a dual-excitation (DEXI) readout (Schmithorst et al., 2014), see Fig. 3 for a sequence timing diagram. The labelling duration and PLD were both set to 1.5s, GRAPPA acceleration (factor = 3) was used with $TE_1 = 10$ ms and $TE_2 = 30$ ms. An effective TR (total repetition time including labelling scheme and both readout periods) of 4.4 s was used to acquire 15 slices, in-plane resolution 3.4 × 3.4 mm and slice thickness 7 mm with a 20% slice gap. A calibration (M_0) image was acquired for ASL quantification with pCASL and background suppression switched off, with TR of 6 s, and TE = 10 ms.

For a subset of volunteers (n = 7, 3 males, mean age 37.4 ± 6.7 years) an additional 8-min black and white visual checkerboard task (reversing at a frequency of 2Hz, alternating between 30 s rest and 30 s stimulus) was performed during pCASL DEXI data acquisition. In each volunteer a T_1-weighted structural image was acquired for grey matter segmentation and to aid registration to standard (MNI) space.

Blood samples were drawn via a finger prick prior to scanning and were analysed with the HemoCue Hb 301 System (HemoCue, Ängelholm, Sweden) to calculate the systemic [Hb] value for each participant. The partial pressures of end-tidal gas concentrations were assumed to be in equilibrium with arterial blood, such that $PaO_2 = P_{ET}O_2$ and $PaCO_2 = P_{ET}CO_2$. Baseline $PaCO_2$ recordings were used to estimate resting blood pH based on the Henderson-Hasselbalch equation (equation (10)), assuming HCO_3^- = 24 mmol/L (Gai et al., 2003).

$$pH = 6.1 + log\{HCO_3^- / (0.03 \cdot PCO_2)\} \quad (10)$$

From which the resting P_{50} was calculated according to the linear correlation, $P_{50} = 221.87–26.37 \times pH$, reported by (Gai et al., 2003). The Severinghaus equation (Severinghaus, 1979) was used to convert PaO_2 recordings into SaO_2 time series, which were then converted to CaO_2 via equation (11).

$$CaO_2 = \varphi \cdot [Hb] \cdot SaO_2 + \varepsilon \cdot PaO_2 \quad (11)$$

where ε is the O_2 plasma solubility (0.0031 ml/mmHg/dL). The T_1 of arterial blood was calculated from a linear fit to SaO_2, PaO_2 and $R_{1,blood}$ in-vivo data presented in (Pilkinton et al., 2012), equation (12).

$$R_{1,blood} = 1.527 \times 10^{-4} \cdot PaO_2 + 0.1713 \cdot (1 - SaO_2) + 0.5848 \quad (12)$$

where $R_{1,blood}$ is the longitudinal relaxation rate of arterial blood in seconds.

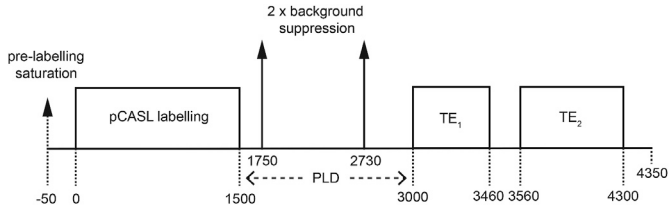

Fig. 3. Pulse sequence timing diagram for dual-excitation pseudo-continuous arterial spin labelling (DEXI-pCASL) acquisition. Sequence timings are in ms to the nearest 5 ms.

2.4. Data analysis

Data were pre-processed using a combination of MATLAB code and FSL (Jenkinson et al., 2012). Motion correction was performed with the FSL MCFLIRT function and spatial smoothing (FWHM = 4.5 mm) of the BOLD data (surround average of TE_2) was performed with SUSAN (Smith and Brady, 1997). ASL data (surround subtraction of TE_1) and M_0 acquisition were spatially smoothed using a 3D Gaussian kernel (FWHM 4.5 mm). DEXI data was registered to the structural T_1 data using FSL's epi-reg tool. Following grey matter segmentation of the structural T_1

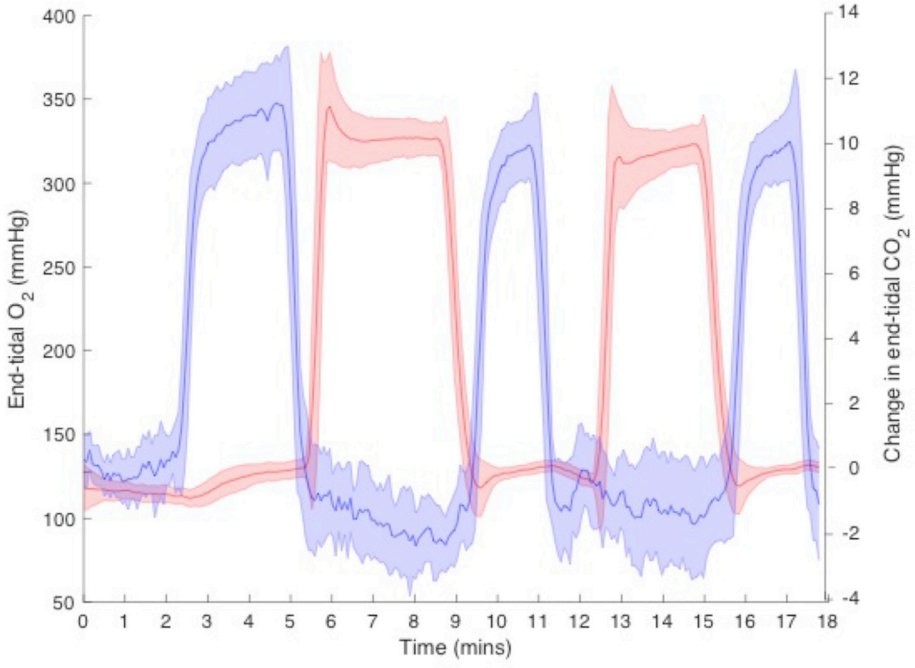

Fig. 2. Mean (solid line) and standard deviation (shaded area) of end-tidal recordings from all subjects included in analysis (n = 16). Absolute value of end-tidal oxygen partial pressure (red) and relative change in end-tidal carbon dioxide partial pressure (mmHg).

image, using FAST (Zhang et al., 2001), grey matter estimates were transformed to native space and used for grey matter masking (threshold of 0.5). DEXI data was masked prior to analysis using a binarised M_0 image to reduce processing time.

End-tidal traces were aligned with the DEXI data via a cross-correlation between $PaCO_2$ and the mean grey matter ASL signal. Measured [Hb] and calculated P_{50} values were used to resample the initial 4D effective diffusivity lookup table to a high-resolution 2D lookup table relating CBF_0 and D_c to OEF, enabling simple linear interpolation to be used during fitting. MATLAB's non-linear least squares minimisation routine (lsqnonlin) was used to simultaneously optimise voxelwise estimates of D_c, OEF_0, CBF_0, κ, and the cerebral vascular reactivity (CVR) by minimising the least squares difference between the acquired data and modelled ASL and BOLD timeseries (MATLAB code for pre-processing of end-tidal traces and parameter estimation is available from 10.5281/zenodo.1285862 and 10.5281/zenodo.1285845). See Fig. 4 for a flow diagram representing the forward model used in the analysis framework. In line with the forward modelling approach previously published (Germuska et al., 2016) regularisation was applied to reduce instability in fitting a non-linear model to the data (see appendix for full details). Briefly, regularisation was applied to D_C and OEF in an adaptive manner to reduce the sensitivity to noise variation across voxels and subjects. The regularisation parameter for oxygen extraction fraction was assumed to be uniform, with a nominal OEF_0 of 0.4. We make the assumption that oxygen diffusivity varies with capillary density (and therefore grey matter partial volume) to impose spatial variation on the diffusivity regularisation. Grey matter partial volume estimates were calculated by normalising an initial perfusion estimate by its maximum value (median value in 100 voxels with greatest signal intensity) and then multiplying by 0.15 ml/100g/mmHg/min. We use an initial perfusion estimate (rather than a segmented structural image) to estimate grey matter partial volume to avoid bias due to segmentation and registration errors. As per our previous work (Germuska et al., 2016), we used digital phantom experiments to determine the optimal level of regularisation for each parameter, OEF and D_C. Additionally, we explored the influence of the SNR on the mean squared error of regularised fits to the simulated data; see the appendix for further details of the simulations.

Visual data was subject to the same pre-processing steps as the

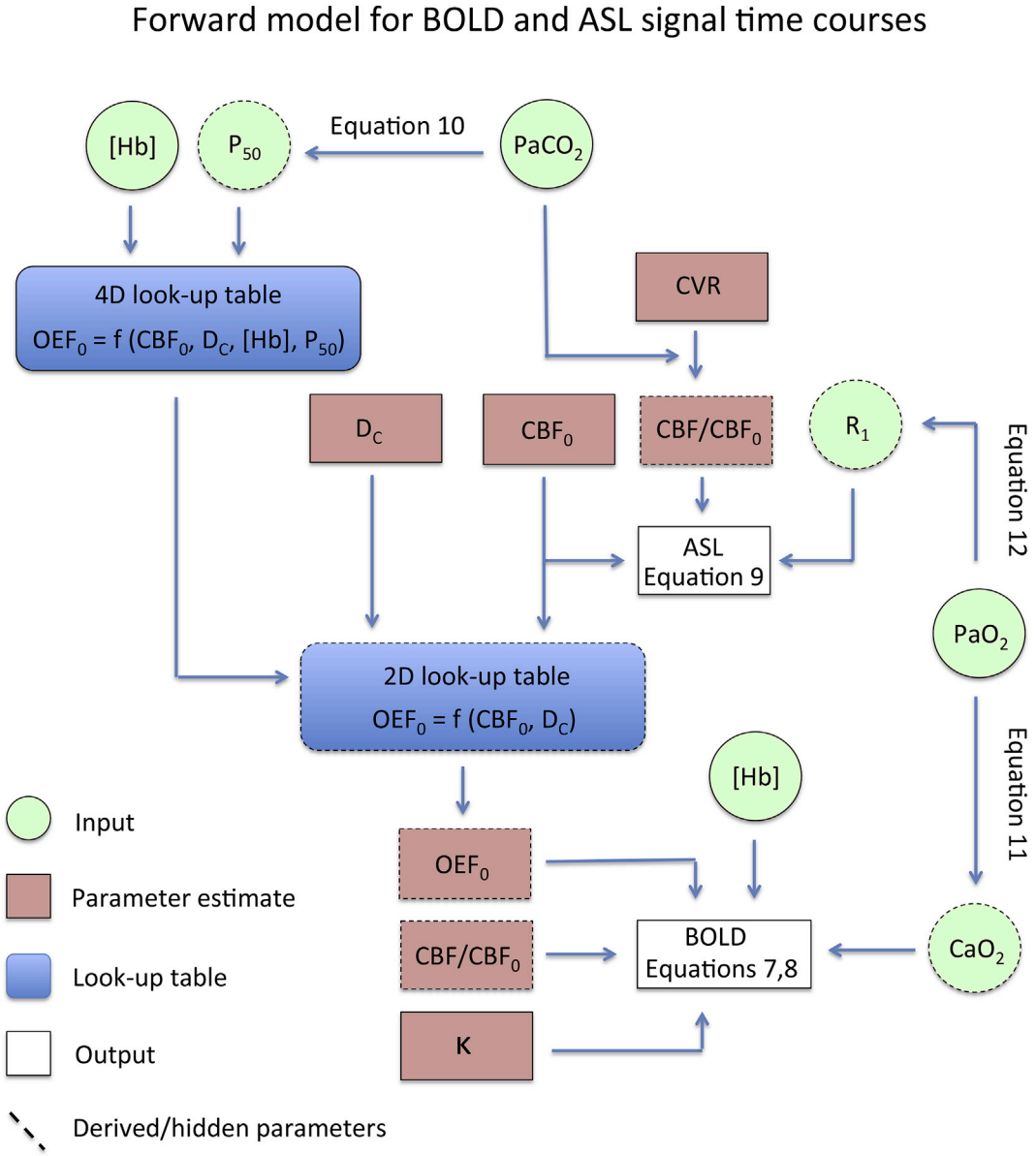

Fig. 4. Flow diagram showing how measured physiological data and estimated parameters are combined to estimate ASL and BOLD signal time courses during parameter estimation. The forward model incorporates oxygen diffusivity modelling into a dual-calibrated fMRI framework.

Table 2
Mean (±standard deviation) systemic and grey matter estimates at baseline, (n = 16).

[Hb] g/dl	P_{50} mmHg	CBF ml/100 g/min	OEF	$CMRO_2$ μmol/100 g/min	D_C ml/100g/mmHg/min	CVR %/mmHg
14.3 ± 1.5	27.1 ± 0.1	55.6 ± 6.3	0.38 ± 0.04	157.4 ± 12.3	0.092 ± 0.009	2.4 ± 0.4

baseline data, additionally it was registered (FLIRT) to baseline data to account for any gross subject motion between the datasets. Percentage change in CBF and the BOLD signals were calculated using FEAT to fit the pre-processed data with the visual paradigm. $CMRO_2$ was calculated both on a voxel-wise basis, and from a grey matter ROI, which was thresholded to include only voxels with significant BOLD and CBF activation (z-stats > 2.3). Because resting data was quantified using a simplified BOLD model (Merola et al., 2016), the standard calibration model (Davis et al., 1998) was modified as per equation (13) to calculate the visual $CMRO_2$.

$$CMRO_2 = CMRO_{2,0} \cdot \left(1 - \frac{\frac{\Delta BOLD}{BOLD_0}}{TE \cdot \kappa \cdot [dHb]_0}\right) \cdot \left(\frac{CBF}{CBF_0}\right)^{1-\theta} \quad (13)$$

Estimates of $CMRO_2$ and CBF during visual activation were used to calculate OEF via the Fick principle, while estimates of D_C were made by inverting the look-up table and assuming constant [Hb] and P_{50}.

3. Results

The mean and standard deviation of baseline $P_{ET}O_2$ and $P_{ET}CO_2$ were 116 ± 5 mmHg and 41.6 ± 3.6 mmHg, the hyperoxic respiratory modulation resulted in an average $P_{ET}O_2$ of 325.2 ± 12.8 mmHg, while hypercapnia produced an average $P_{ET}CO_2$ of 51.7 ± 3.5 mmHg. Three subjects did not return to a stable $P_{ET}CO_2$ baseline during the medical air periods of the DEXI acquisition; this was judged to be a deviation of greater than 4 mmHg below the starting value. These subjects were excluded from further analysis. The mean increase in grey matter CBF during hypercapnia was 24.0 ± 3.7%. Group average values of the resting grey matter physiological parameters are reported in Table 2.

The mean grey matter value of the effective diffusivity was 0.092 ± 0.01 ml/100g/mmHg/min, or 3.62 ± 0.39 μmol/100g/mmHg/min, which is in good agreement with the PET measurements made by (Ibaraki et al., 2010) and (Vafaee and Gjedde, 2000) who report value of 3.38 and 4.09 respectively. Baseline values of $CMRO_2$ are strongly correlated with the effective oxygen diffusivity ($R^2 = 0.81$, $p < 0.01$), across participants, as shown in Fig. 5a. This coupling between $CMRO_2$ and oxygen diffusivity is also demonstrated within subjects, with a clear spatial similarity between the baseline parameter maps. Example resting parameter maps (CBF_0, $CMRO_{2,0}$ and $D_{c,0}$) for an individual subject are shown in Fig. 6. The similarity between the parameter maps is clear, with the maps of effective diffusivity closely following $CMRO_2$.

While the effective diffusivity appears to be strongly coupled to resting demand, we observed a strong negative correlation between baseline oxygen delivery ($CaO_2 \times CBF$) and oxygen extraction ($R^2 = 0.57$, $p < 0.01$) (Fig. 5b). This is consistent with previous findings of a strong negative correlation between OEF_0 and CBF_0 (Germuska et al., 2016; Lu et al., 2008) when [Hb] was assumed to be constant. By incorporating a measured [Hb] in the calculation of CaO_2, the correlation with oxygen delivery is revealed; demonstrating the action of the cerebrovascular system to maintain a tightly controlled resting metabolic rate of oxygen consumption across participants.

To investigate the observed linear relationship between $CMRO_{2,0}$ and $D_{C,0}$, we solved the inverse model with fixed [Hb] (14.3 g/dl), P_{50} (27.1 mmHg), and $CaO_{2,0}$ (0.189 ml O2/ml blood). By doing so we are able to examine the modelled co-variance between $CMRO_{2,0}$ and CBF_0 in isolation of other physiological factors, see Fig. 7. The analysis suggests a small positive correlation between CBF_0 and $CMRO_{2,0}$ is required to produce a strictly linear relationship between $CMRO_{2,0}$ and $D_{C,0}$, which agrees well with the in-vivo data ($p < 0.05$ for a paired *t*-test comparison between the predicted CBF_0 and the normalised CBF_0 estimates ($CaO_{2,0}$ x (CBF_0/0.189)). However, if the effective oxygen diffusivity is considered to be a constant physiological parameter, as is sometimes assumed (Vafaee et al., 2012), then a significant non-linear (exponential) relationship is predicted between CBF_0 and $CMRO_{2,0}$. Finally, we explored a hypothetical scenario in which the inverse of the correlation observed in this study exists between $CMRO_{2,0}$ and $D_{C,0}$. This scenario requires a much larger increase in CBF_0 with $CMRO_{2,0}$, but it is still mathematically and physiologically feasible to produce such a relationship. This analysis highlights the fact that even though $D_{C,0}$ and $CMRO_{2,0}$ appear to be coupled (in the examined cohort of young healthy volunteers) they provide complementary information, with $CMRO_2$ reporting on the rate of oxygen consumption and D_C reporting on the ability of the capillary network to supply oxygen to the tissue/mitochondria. The coupling between these parameters is likely the result of the expected correlation between microvascular structure (diffusivity) and function (metabolism).

During visual simulation cerebral blood flow increased within the defined ROI (in the primary visual cortex, as expected) by 21.4 ± 4.6%, while $CMRO_2$ increased by 15.1 ± 3.5%, resulting in a CBF to $CMRO_2$ coupling ratio of 1.44 ± 0.24. The effective oxygen diffusivity was found to increase by 12.5 ± 3.6%. The $CMRO_2$ and diffusivity increases are of a similar magnitude to those observed with PET measurements using a 4Hz yellow-blue contrast-reversing checkerboard, where $CMRO_2$ and oxygen diffusivity were found to increase by 14.9% and 9.0% respectively. Fig. 8 shows the mean (n = 7) absolute change in physiological parameters evoked by the visual stimulus overlaid onto the selected slice in standard (MNI) space. Changes in diffusivity are co-localised with changes in $CMRO_2$, whereas changes in CBF are more widespread.

Fig. 9 shows the correlation between the average $CMRO_2$ and effective diffusivity within the visual ROI at baseline (crosses) and during activation (diamonds) for each participant. It is clear from the graph that the coupling between demand and diffusivity, that was previously observed in the grey matter baseline data, is preserved during activation, R^2 (baseline) = 0.95, R^2 (activation) = 0.96, $p < 0.01$ for both datasets.

Under the assumption that P_m is minimal and the effective permeability is held constant during activation, the apparent change in capillary blood volume is linearly related to the effective diffusivity (see equations (5) and (6)). Thus, we can calculate the apparent flow-volume coupling relationship, $CBV/CBV_0 = (CBF/CBF_0)^{\eta}$, implied from the diffusivity data. Using this line of reasoning we find that a coupling constant of 0.62 ± 0.13 is required, relating the 21% flow change to an apparent 12.5% volume increase. This result agrees surprisingly well with in-vivo observations of functional capillary vasodilation. Where the 6.7% increase in capillary diameter observed by (Hall et al., 2014) was calculated to produce a 19% increase in blood flow according to Poiseuille's law. Assuming constant capillary length this observation would predict a flow-volume coupling exponent of approximately 0.75 for their data.

4. Discussion and conclusions

In this manuscript we have presented a novel framework for the

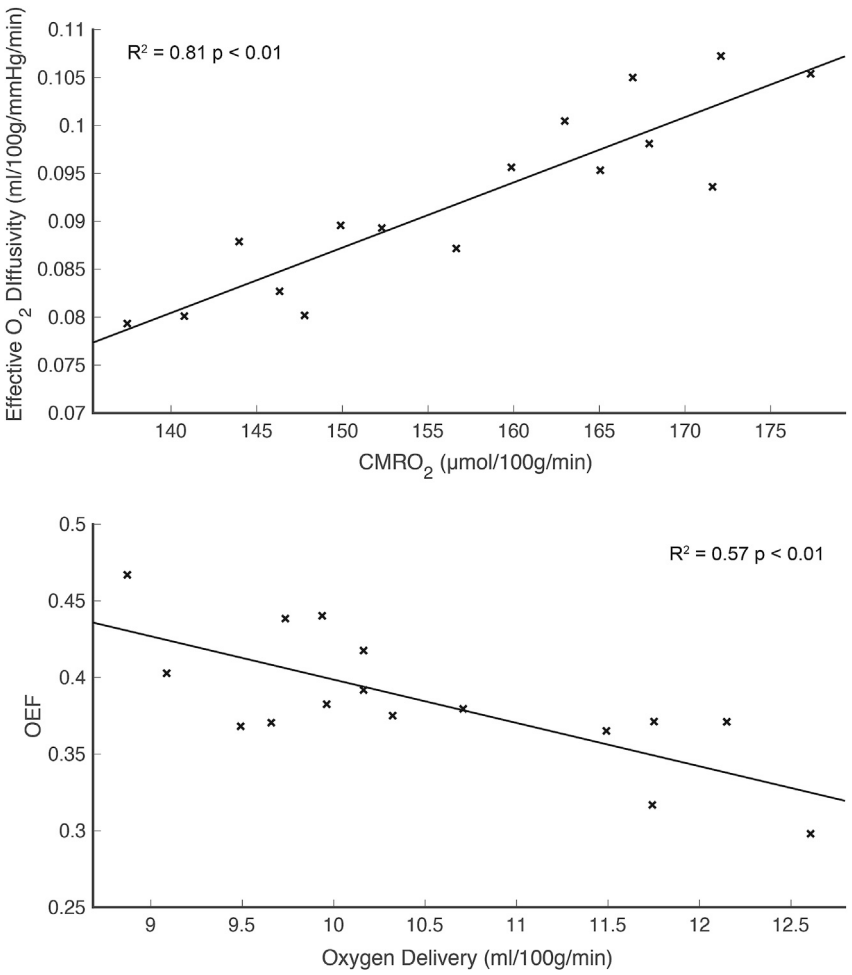

Fig. 5. Scatter plots of whole brain grey matter parameter estimates at baseline for each subject (n = 16). Top panel (A) demonstrates a strong correlation between baseline metabolic oxygen consumption and effective oxygen diffusivity. Bottom panel (B) shows a strong negative correlation between oxygen extraction and oxygen delivery, such that delivery is elevated when OEF is low.

analysis of dual-calibrated data to produce simultaneous estimates of $CMRO_2$ and effective oxygen diffusivity. The combined analysis of these two physiological parameters has the potential to provide useful insight into the underlying metabolic and vascular responses to different brain states and disease. The method was applied at rest and in combination with a visual task. The resting data showed a tight coupling between grey matter diffusivity and the basal rate of oxygen metabolism. This result is expected in the healthy brain, as there is significant evidence of a structural link between the density of capillaries (a significant determinant of the effective diffusivity) and metabolism (Gjedde et al., 1990; Harrison et al., 2002; Sette et al., 1989).

The effective diffusivity was also found to increase during functional activation, with a 12.5% increase in diffusivity being associated with a 15.1% increase in $CMRO_2$ and 21.4% increase in CBF. The coupling ratio between CBF and $CMRO_2$, 1.44, is at the lower end of *in-vivo* observations, which typically range from 1.3 to 5 for MRI methodologies (Leithner and Royl, 2014). Thus, the change in effective diffusivity is likely to be at the higher end of the expected range (in order to meet the oxygen demands of the elevated $CMRO_2$ in the absence of a greater increase in CBF). Possible mechanisms to provide such an increase in effective diffusivity include a direct increase in capillary blood volume (Hyder et al., 1998), a homogenisation of capillary flow heterogeneity (Jespersen and Ostergaard, 2012), a reduction in the mitochondrial oxygen tension (Gjedde et al., 2005), or a high resting tissue oxygen tension (Buxton, 2010). While each of these factors could play a role in modulating the diffusivity of the capillary network, *in-vivo* measurements suggest that tissue oxygenation initially increases during functional activation and then normalises to a level slightly above its resting value (Ances et al., 2001). Thus, it is unlikely that there is a significant reduction in mitochondrial oxygen tension, which would be expected to lower tissue oxygenation rather than increase it. Alternatively, a high resting mitochondrial oxygen tension would result in a small vessel-to-tissue PO_2 gradient, which, as highlighted by (Hyder et al., 2000), increases the effectiveness by which CBF can increase O_2 delivery to the tissue. Our model predicts that the mitochondrial oxygen tension would need to be unrealistically high, approximately 30 mmHg to explain the $CBF/CMRO_2$ increases observed in this study. While there is uncertainty in the value of P_m in the human brain, animal studies suggest that it is between 0.1 and 10 mmHg (Herman et al., 2006), thus a significant resting mitochondrial oxygen tension is unlikely. An alternative explanation explored in this paper is that there is a direct increase in capillary blood volume, potentially mediated by capillary pericytes; which have been demonstrated to alter capillary volume independently of arteriolar dilation (Mishra et al., 2016) and appear to play a significant role in neurovascular coupling (Kisler et al., 2017).

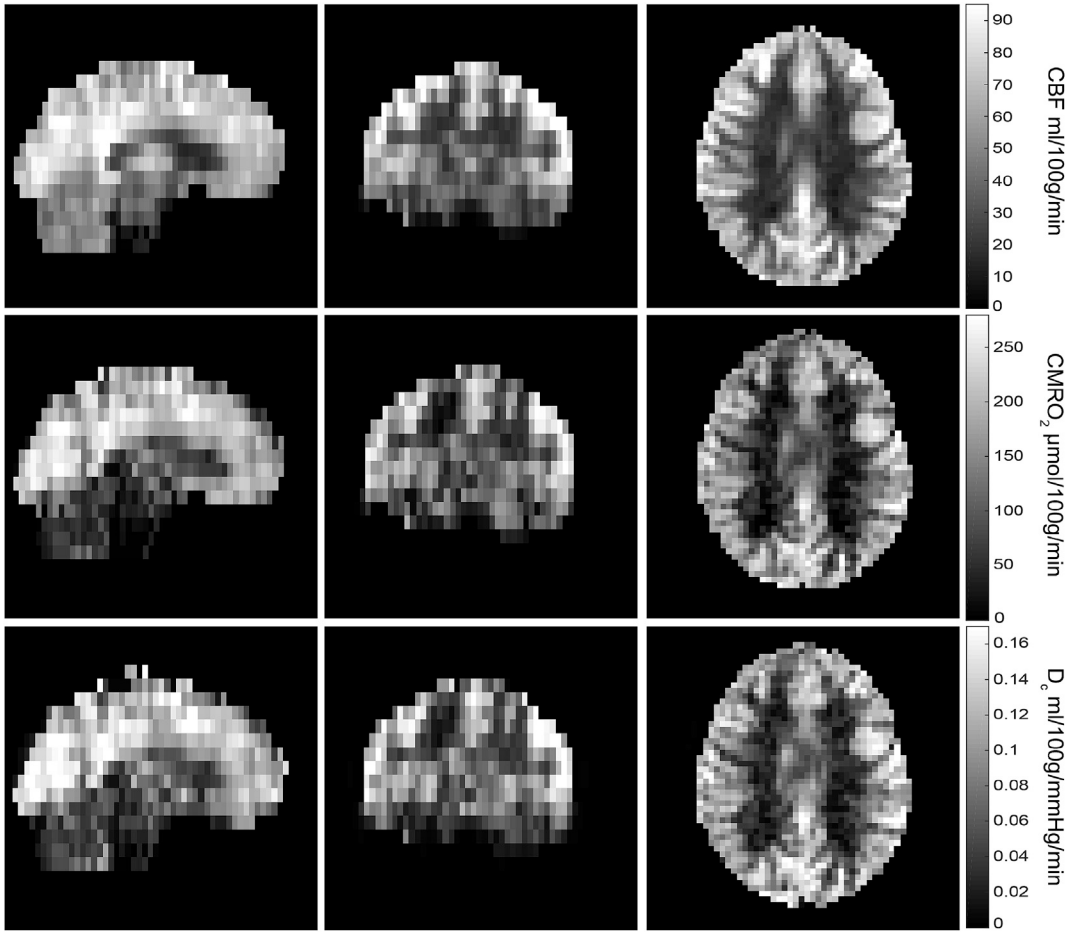

Fig. 6. Example baseline (CBF_0, $CMRO_{2,0}$ and $D_{c,0}$) parameter maps for an individual subject. The spatial similarity between oxygen diffusivity and the basal rate of oxygen metabolism is evidence of a strong structural-functional coupling between the two parameters in the basal state.

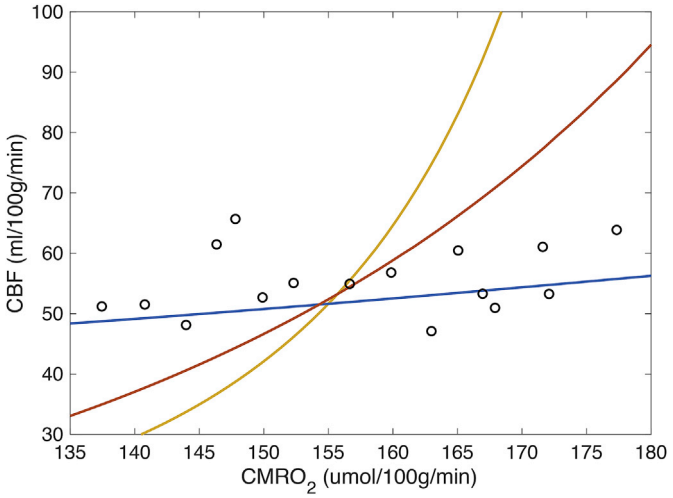

Fig. 7. Modelled relationship between $CMRO_{2,0}$ and CBF_0 for linear increase in $D_{C,0}$ with $CMRO_{2,0}$ (blue), constant $D_{C,0}$ (orange), and linear decrease in $D_{C,0}$ with $CMRO_{2,0}$ (yellow). In-vivo $CMRO_{2,0}$ and normalised CBF_0 ($CaO_{2,0}{\cdot}CBF_0$/0.189), mean grey matter values overlaid (circles).

For a given rate of perfusion, an increase in capillary volume would increase the mean transit time for blood to transverse the capillary network, producing a proportional increase in the effective diffusivity, and thus enabling greater extraction of the oxygen from the capillary bed. Our data suggest that a flow-volume coupling exponent of approximately 0.62 is required in the capillaries to provide the observed increase in effective diffusivity during visual stimulation. The implied 12.5% increase in capillary blood volume agrees well with the data and analysis presented by (Hall et al., 2014) in the mouse brain, suggesting this is a plausible explanation for the observed increase in diffusivity. Indeed more recent studies in the mouse brain suggest that such an increase in capillary blood volume is well within the range of normal physiological responses, where capillary volume has been found to increase by 10–26% during functional activation depending on the baseline diameter (Ito et al., 2017).

Although modulation of capillary blood volume appears to be sufficient to provide local control of capillary diffusivity, we cannot rule out a contribution from flow heterogeneity (Jespersen and Ostergaard, 2012), which is likely to be reduced during functional activation where smaller capillaries have been observed to dilate more than larger capillaries in rat (Kleinfeld et al., 1998; Stefanovic et al., 2008). However, the influence of flow heterogeneity is known to be dependent on the transit time distribution (Angleys et al., 2015), and confounding factors such as the heterogeneity of [Hb] have not been considered in the modelling, thus it is still unclear if this theoretical model of control is realised *in-vivo*.

As previously discussed, there is unlikely to be a significant resting P_m in the studied cohort, meaning the assumption of negligible P_m is

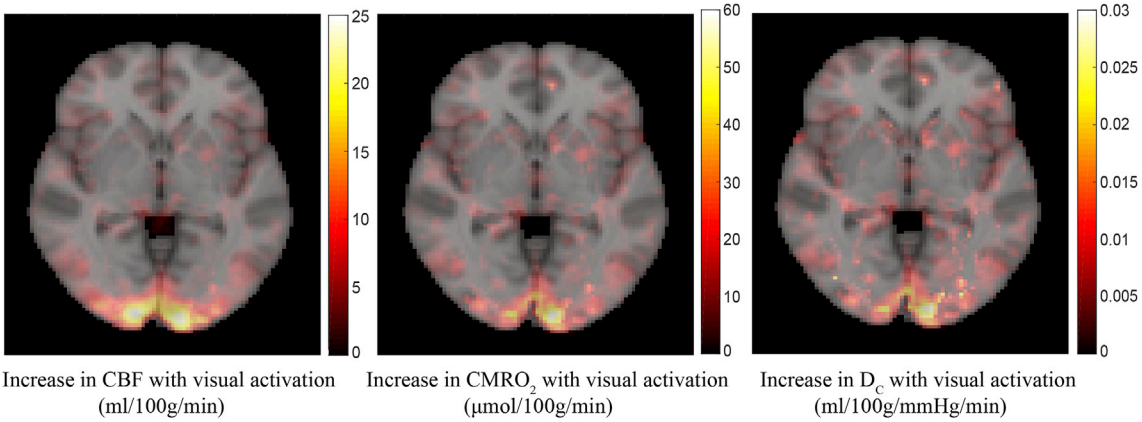

Fig. 8. Overlay of the mean absolute change in CBF, $CMRO_2$, and effective oxygen diffusivity evoked by the visual checkerboard stimulus for n = 7 subjects.

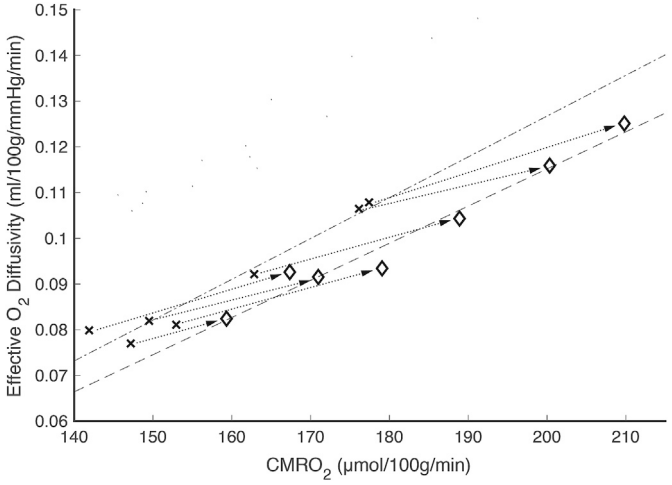

Fig. 9. Summary plot of visual ROI data for $CMRO_2$ and effective oxygen diffusivity (including resting and activation data for n = 7 subjects). A tight correlation between $CMRO_2$ and effective diffusivity is observed both at baseline (crosses) and during activation (diamonds), indicative of a tight coupling between the effective diffusivity and oxygen demand. The dashed lines are lines of best fit (linear regression) the dotted lines connect baseline and activation data for each subject.

unlikely to impact the results. However, this may not always be true. In theory P_m could increase in the presence of significant mitochondrial dysfunction due to the lack of oxygen uptake in the mitochondria. Currently the only direct evidence we are aware of for an increase in tissue (and therefore most likely mitochondrial) oxygen tension during mitochondrial dysfunction is from simulated dysfunction (due to a cyanide infusion) in piglets (Nielsen et al., 2013). However, there is increasing evidence of mitochondrial dysfunction in a number of neurodegenerative diseases such as Parkinson's disease (Powers et al., 2008) and Alzheimer's disease (Wang et al., 2014). Therefore, it should be highlighted that reductions in basal D_C may not always correspond to a purely vascular origin and may also incorporate mitochondrial dysfunction.

In line with our previously published methods for analysis of dual-calibrated data (Germuska et al., 2016; Wise et al., 2013) we have included priors to stabilise the fitting process (see appendix). In the current implementation the priors are incorporated into parameter estimates via adaptive regularisation. Whenever priors are used to guide the fitting process there is always a trade off to be made between overfitting (not enough regularisation) and underfitting (too much regularisation). Digital phantom simulations were used to optimise the amount of regularisation and balance this trade-off. The proposed method employs regularisation on two parameters, the resting OEF and the effective diffusivity. In the case of underfitting we would expect the results to closely follow the prior, thus there would be little variation in OEF or the effective diffusivity between subjects. In contrast we find that OEF is highly correlated with resting oxygen delivery, and the effective diffusivity is tightly coupled to the resting $CMRO_2$. Thus, it is unlikely that the results are significantly affected by underfitting. While we cannot rule out overfitting of the data, the appearance of the parameter maps is physiologically plausible and they do not suffer from significant instability within the grey matter. To further explore the influence of the proposed framework on the parameter estimates we performed simulations where D_C was not estimated. In this implementation OEF was estimated directly as in (Germuska et al., 2016), and thus no regularisation was/could be placed on D_C. These simulations (see appendix) showed similar levels of error to the proposed method, albeit with slightly increase RMSE in OEF estimates at low tSNR.

In conclusion, we have presented an MRI method for mapping the effective oxygen diffusivity of the capillary bed in combination with metabolic oxygen consumption. The method shows good agreement with PET literature and inferred changes in capillary blood volume are in agreement with two-photon laser microscopy measurements in animals, however, direct validation of the method is still outstanding. The proposed method is non-invasive and can be performed in a short timeframe. Previous measurements of effective oxygen diffusivity suggest it may be a valuable tool to understand the brain's response to altered oxygen supply and demand. Thus, the introduction of this method could offer a useful insight into a range of conditions and diseases with altered metabolism or vascular function.

Acknowledgements

We would like to thank Wellcome for supporting this work: Wellcome Strategic Award, 'Multi-scale and multi-modal assessment of coupling in the healthy and diseased brain', grant reference 104943/Z/14/Z (RW, MG, CF and RS). RW also thanks the Higher Education Funding Council for Wales for support. KM is supported by Wellcome grant 200804/Z/16/Z. TO is supported by the Royal Academy of Engineering and Wellcome Centre for Integrative Neuroimaging is supported by core funding from Wellcome (203139/Z/16/Z). We are also grateful to Takuya Hayashi for the helpful exchanges discussing the compartmental modelling of oxygen exchange.

Appendix. Digital phantom simulations

We can model the observed MRI data, ASL and BOLD signals that we wish to fit, via equation (A1).

$$Y_i = f(w_i, X) + e_i,\ e \sim N(0, \sigma^2) \tag{A1}$$

Where Y represents the observed MRI signal data, X represents the corresponding physiological traces and their derived parameters (see Fig. 2), w is a vector of physiological parameters, e is signal noise with zero mean and an unknown variance σ^2, and *i* is the voxel index.

In order to estimate the physiological parameters, *w*, we perform regularised non-linear least squares minimisation (via MATLAB's lsqnonlin function), as defined by equation (A2).

$$w_{i|RLS} = \min_{w}\left(\| f(w_i, X) - Y_i\|_2^2 + \lambda\widehat{\sigma}_i^2 \| w_i^{'} - v_i\|_2^2 \right) \tag{A2}$$

Where $w_{i|RLS}$ is the regularised least squares estimate of the physiological parameters at the *i*th voxel. λ is a vector of regularisation coefficient, $\widehat{\sigma}^2$ is a voxelwise estimate of noise variance (calculated from the variance of the residuals), w' is a vector comprising the parameter estimates for D_C and OEF, and v is a vector of the corresponding expected values. The expected value for OEF is set to 0.4 for all voxels (representing a nominal OEF near the mid-point of the physiological range), while the expected value for diffusivity estimates are linearly related to voxel-wise grey matter partial volume estimates. In this way we impose a prior belief that the effective diffusivity will be linearly related to grey matter content (due to the associated relationship with CBV). The expected value for pure grey matter voxels is set to a nominal D_C value of 0.15 ml/100g/mmHg/min, corresponding to an OEF of 0.35 (Ibaraki et al., 2008), when Hb = 0.15 g/ml, P_{50} = 26 mmHg, and CBF = 90 ml/100 g/min (Asllani et al., 2008).

Because the noise variance is estimated on a voxel-wise basis the regularisation is spatially adaptive; with greater regularisation applied when the noise variance estimate is greater. It should also be noted that the magnitude of the regularisation reduces as the minimisation routine approaches the solution, which has been shown to reduce the bias at convergence (Hong et al., 2017). The value of the regularisation coefficients λ_{Dc} and λ_{OEF}, which define the vector λ, were determined from digital phantom simulations, as described below.

Simulated phantoms were created with 245 time points (matching the in-vivo acquisition), for both the ASL and BOLD data, and 4200 elements. Effective diffusivity values were randomly chosen in the range 0.03–0.18, OEF values were assigned values from 0.25 to 0.55, Hb was set to 0.15 g/ml, P_{50} was set to 26 mmHg, if any combination of values implied a CBF below 20 or above 150 ml/100 g/min (according to the flow-diffusion modelling) another value was randomly chosen until this criteria was met. The tSNR of the simulated data was set to match that of the acquired data (after spatial smoothing), which were approximately 4.5 for the ASL data and 150 for the BOLD data. In order to match to in-vivo noise statistics, simulated ASL and BOLD time series were band-pass filtered with a second order infinite impulse response filter using the MATLAB 'designfilt' function. The relative bandpass frequencies were 0.08–0.2 for the ASL data and 0.01 to 0.2 for the BOLD data (pass band ripple 1 dB in each case).

The RMS error in OEF and D_C estimates were calculated for varying levels of regularisation under two conditions; with regularisation applied only to OEF and with regularisation applied only to D_C. Thus, optimising the required regularisation for each parameter separately. By analogy to the standard L-curve method (Hansen, 1992), the optimal level of regularisation was chosen to be the maximum of the curvature of the λ vs RMS error plot (see figures A1 and A2). Thus, selecting the transition point above which further regularisation ceases to provide significant reductions in RMS error. Because we are optimising the regularisation for two parameters (and in two conditions), there are two transition points to choose between in each condition. To minimise the chances of underfitting we chose the point that corresponds to the smallest amount of regularisation in each case.

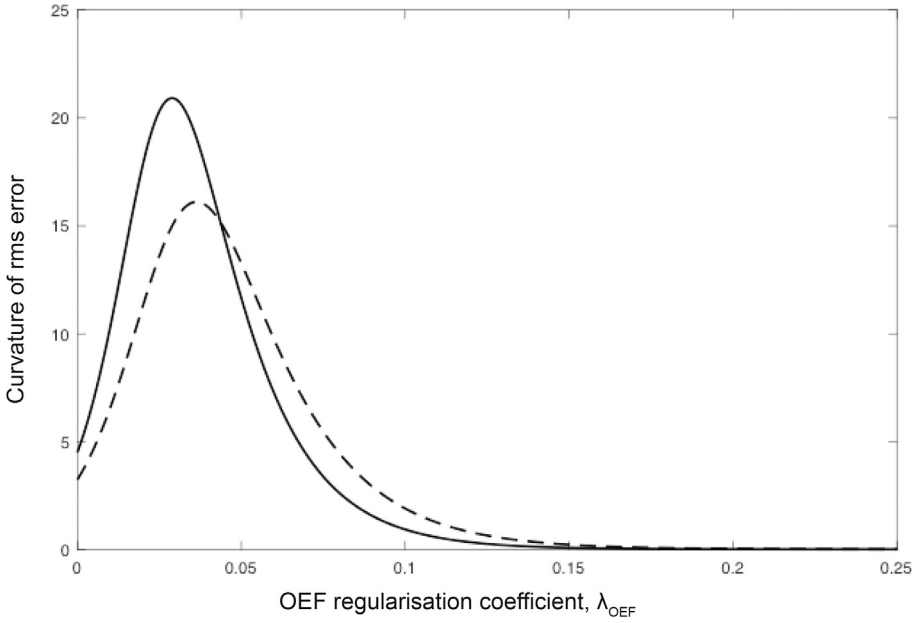

Fig. A1. Plot of λ_{OEF} vs. curvature of rms error for effective diffusivity (solid line) and OEF (dashed line). The curvature of the diffusivity error reaches a maximum before the curvature of the OEF error, therefore this point (0.03) was chosen for lambda.

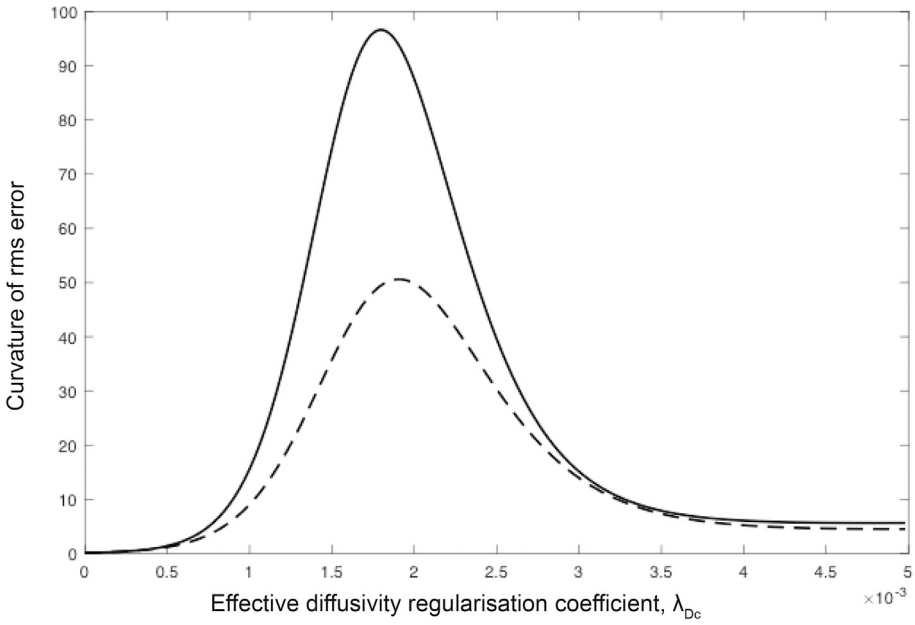

Fig. A2. Plot of λ_{Dc} vs. curvature of rms error for effective diffusivity (solid line) and OEF (dashed line). The curvature of the diffusivity error reaches a maximum marginally before the curvature of the OEF error. The peak of the D_C curvature is at approximately 1.8×10^{-3}, and therefore this value is used to set the level of regularisation for D_C estimates.

Having optimised λ for a fixed tSNR we explored the noise sensitivity of OEF and D_C estimates for ASL tSNR ranging from 0.5 to 8.5 (BOLD tSNR was linearly scaled with ASL tSNR and so ranged from 17 to 280). The results of these simulations are shown in figure A3 and demonstrate a non-linear increase N-RMSE for both OEF and D_C as the tSNR is reduced. It is apparent from the simulation that there is less uncertainty in OEF estimates, with a 15% error occurring for a tSNR of approximately 3, while D_C requires a tSNR of approximately 5 to achieve the same level of uncertainty. For comparison with previous methods, which do not fit for D_C, we have also included the error in OEF estimates when fitting for OEF directly. This is equivalent to the implementation in (Germuska et al., 2016), but with adaptive (rather than fixed) regularisation placed only on OEF. The regularisation for this approach was tuned to match the current implementation when the ASL tSNR = 4.5. As can be seen from the plot, the error in OEF estimates are similar to the newly proposed method, with a slight reduction for high tSNR and a decrease in performance for low tSNR. This decrease in performance for low tSNR is likely due to the convergence of the fit to a uniform prior, rather than a prior informed by the estimate of baseline CBF.

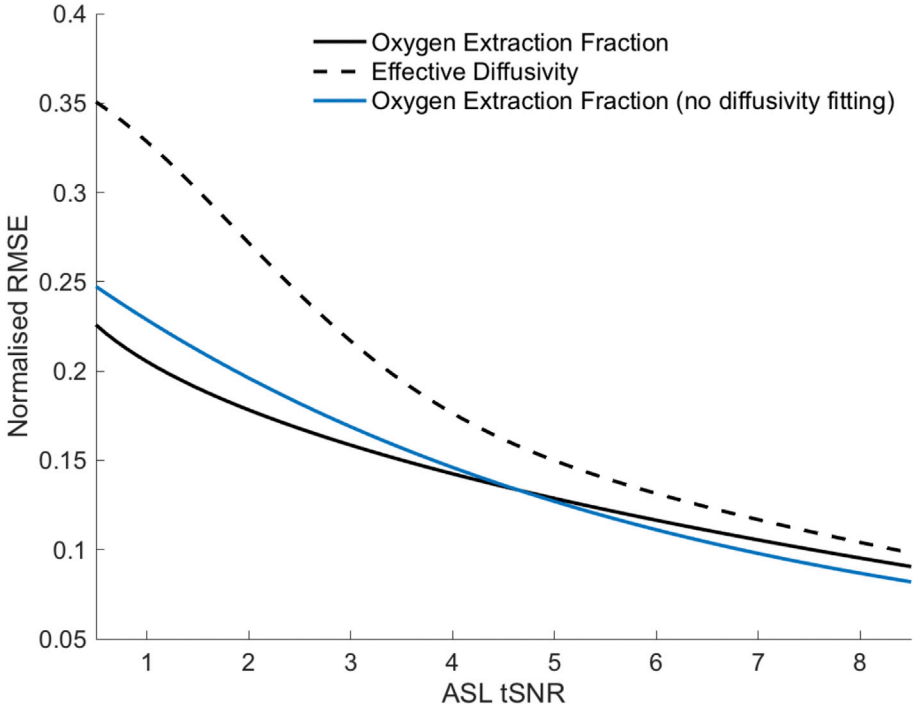

Fig. A3. Plot of normalised RMSE in OEF and D_C predicted with varying levels of tSNR (ASL) from digital phantom simulations.

References

Alsop, D.C., Detre, J.A., Golay, X., Gunther, M., Hendrikse, J., Hernandez-Garcia, L., Lu, H., MacIntosh, B.J., Parkes, L.M., Smits, M., van Osch, M.J., Wang, D.J., Wong, E.C., Zaharchuk, G., 2015. Recommended implementation of arterial spin-labeled perfusion MRI for clinical applications: a consensus of the ISMRM perfusion study group and the European consortium for ASL in dementia. Magn. Reson. Med. 73, 102–116.

Ances, B.M., Buerk, D.G., Greenberg, J.H., Detre, J.A., 2001. Temporal dynamics of the partial pressure of brain tissue oxygen during functional forepaw stimulation in rats. Neurosci. Lett. 306, 106–110.

Angleys, H., Ostergaard, L., Jespersen, S.N., 2015. The effects of capillary transit time heterogeneity (CTH) on brain oxygenation. J. Cerebr. Blood Flow Metabol. 35, 806–817.

Asllani, I., Borogovac, A., Brown, T.R., 2008. Regression algorithm correcting for partial volume effects in arterial spin labeling MRI. Magn. Reson. Med. 60, 1362–1371.

Bulte, D.P., Kelly, M., Germuska, M., Xie, J., Chappell, M.A., Okell, T.W., Bright, M.G., Jezzard, P., 2012. Quantitative measurement of cerebral physiology using respiratory-calibrated MRI. Neuroimage 60, 582–591.

Buxton, R.B., 2010. Interpreting oxygenation-based neuroimaging signals: the importance and the challenge of understanding brain oxygen metabolism. Front. Neuroenergetics 2, 8.

Buxton, R.B., Frank, L.R., 1997. A model for the coupling between cerebral blood flow and oxygen metabolism during neural stimulation. J. Cerebr. Blood Flow Metabol. 17, 64–72.

Davis, T.L., Kwong, K.K., Weisskoff, R.M., Rosen, B.R., 1998. Calibrated functional MRI: mapping the dynamics of oxidative metabolism. Proc. Natl. Acad. Sci. U. S. A. 95, 1834–1839.

Duling, B.R., Kuschinsky, W., Wahl, M., 1979. Measurements of the perivascular PO2 in the vicinity of the pial vessels of the cat. Pflügers Archiv 383, 29–34.

Gai, X., Taki, K., Kato, H., Nagaishi, H., 2003. Regulation of hemoglobin affinity for oxygen by carbonic anhydrase. J. Lab. Clin. Med. 142, 414–420.

Gauthier, C.J., Desjardins-Crepeau, L., Madjar, C., Bherer, L., Hoge, R.D., 2012. Absolute quantification of resting oxygen metabolism and metabolic reactivity during functional activation using QUO2 MRI. Neuroimage 63, 1353–1363.

Germuska, M., Merola, A., Murphy, K., Babic, A., Richmond, L., Khot, S., Hall, J.E., Wise, R.G., 2016. A forward modelling approach for the estimation of oxygen extraction fraction by calibrated fMRI. Neuroimage 139, 313–323.

Gjedde, A., Johannsen, P., Cold, G.E., Ostergaard, L., 2005. Cerebral metabolic response to low blood flow: possible role of cytochrome oxidase inhibition. J. Cerebr. Blood Flow Metabol. 25, 1183–1196.

Gjedde, A., Kuwabara, H., Hakim, A.M., 1990. Reduction of functional capillary density in human brain after stroke. J. Cerebr. Blood Flow Metabol. 10, 317–326.

Gjedde, A., Poulsen, P.H., Ostergaard, L., 1999. On the oxygenation of hemoglobin in the human brain. Adv. Exp. Med. Biol. 471, 67–81.

Hall, C.N., Reynell, C., Gesslein, B., Hamilton, N.B., Mishra, A., Sutherland, B.A., O'Farrell, F.M., Buchan, A.M., Lauritzen, M., Attwell, D., 2014. Capillary pericytes regulate cerebral blood flow in health and disease. Nature 508, 55–60.

Hansen, C., 1992. Analysis of discrete Ill-posed problems by means of the L-curve. SIAM Rev. 34, 561–580.

Harrison, R.V., Harel, N., Panesar, J., Mount, R.J., 2002. Blood capillary distribution correlates with hemodynamic-based functional imaging in cerebral cortex. Cerebr. Cortex 12, 225–233.

Hayashi, T., Kudomi, N., Teramoto, N., Watabe, H., Enmi, J., Kim, K., Iida, H., 2004. A physiological model for cerebral oxygen delivery and consumption and effective oxygen diffusibility evaluated by PET. Int. Congr. 1265, 228–237.

Hayashi, T., Watabe, H., Kudomi, N., Kim, K.M., Enmi, J., Hayashida, K., Iida, H., 2003. A theoretical model of oxygen delivery and metabolism for physiologic interpretation of quantitative cerebral blood flow and metabolic rate of oxygen. J. Cerebr. Blood Flow Metabol. 23, 1314–1323.

Herman, P., Trubel, H.K., Hyder, F., 2006. A multiparametric assessment of oxygen efflux from the brain. J. Cerebr. Blood Flow Metabol. 26, 79–91.

Hong, B., Koo, J., Saoatto, S., 2017. Multi-label Segmentation via Residual-driven Adaptive Regularization arXiv:1702.08336.

Hoppeler, H., Kayar, S.R., 1988. Capillarity and oxidative capacity of muscles. Physiology 3, 113–116.

Hudetz, A.G., 1999. Mathematical model of oxygen transport in the cerebral cortex. Brain Res. 817, 75–83.

Hyder, F., Kennan, R.P., Kida, I., Mason, G.F., Behar, K.L., Rothman, D., 2000. Dependence of oxygen delivery on blood flow in rat brain: a 7 tesla nuclear magnetic resonance study. J. Cerebr. Blood Flow Metabol. 20, 485–498.

Hyder, F., Shulman, R.G., Rothman, D.L., 1998. A model for the regulation of cerebral oxygen delivery. J. Appl. Physiol. 1985 (85), 554–564.

Ibaraki, M., Miura, S., Shimosegawa, E., Sugawara, S., Mizuta, T., Ishikawa, A., Amano, M., 2008. Quantification of cerebral blood flow and oxygen metabolism with 3-dimensional PET and 15O: validation by comparison with 2-dimensional PET. J. Nucl. Med. 49, 50–59.

Ibaraki, M., Shinohara, Y., Nakamura, K., Miura, S., Kinoshita, F., Kinoshita, T., 2010. Interindividual variations of cerebral blood flow, oxygen delivery, and metabolism in relation to hemoglobin concentration measured by positron emission tomography in humans. J. Cerebr. Blood Flow Metabol. 30, 1296–1305.

Ito, H., Takuwa, H., Tajima, Y., Kawaguchi, H., Urushihata, T., Taniguchi, J., Ikoma, Y., Seki, C., Ibaraki, M., Masamoto, K., Kanno, I., 2017. Changes in effective diffusivity for oxygen during neural activation and deactivation estimated from capillary diameter measured by two-photon laser microscope. J. Physiol. Sci. 67, 325–330.

Jenkinson, M., Beckmann, C.F., Behrens, T.E., Woolrich, M.W., Smith, S.M., 2012. Fsl. Neuroimage 62, 782–790.

Jespersen, S.N., Ostergaard, L., 2012. The roles of cerebral blood flow, capillary transit time heterogeneity, and oxygen tension in brain oxygenation and metabolism. J. Cerebr. Blood Flow Metabol. 32, 264–277.

Kisler, K., Nelson, A.R., Rege, S.V., Ramanathan, A., Wang, Y., Ahuja, A., Lazic, D., Tsai, P.S., Zhao, Z., Zhou, Y., Boas, D.A., Sakadzic, S., Zlokovic, B.V., 2017. Pericyte degeneration leads to neurovascular uncoupling and limits oxygen supply to brain. Nat. Neurosci. 20, 406–416.

Kleinfeld, D., Mitra, P.P., Helmchen, F., Denk, W., 1998. Fluctuations and stimulus-induced changes in blood flow observed in individual capillaries in layers 2 through 4 of rat neocortex. Proc. Natl. Acad. Sci. U. S. A. 95, 15741–15746.

Leithner, C., Royl, G., 2014. The oxygen paradox of neurovascular coupling. J. Cerebr. Blood Flow Metabol. 34, 19–29.

Lu, H., Zhao, C., Ge, Y., Lewis-Amezcua, K., 2008. Baseline blood oxygenation modulates response amplitude: physiologic basis for intersubject variations in functional MRI signals. Magn. Reson. Med. 60, 364–372.

Merola, A., Murphy, K., Stone, A.J., Germuska, M.A., Griffeth, V.E.M., Blockley, N.P., Buxton, R.B., Wise, R.G., 2016. Measurement of oxygen extraction fraction (OEF): an optimized BOLD signal model for use with hypercapnic and hyperoxic calibration. Neuroimage 129, 159–174.

Mintun, M.A., Lundstrom, B.N., Snyder, A.Z., Vlassenko, A.G., Shulman, G.L., Raichle, M.E., 2001. Blood flow and oxygen delivery to human brain during functional activity: theoretical modeling and experimental data. Proc. Natl. Acad. Sci. U. S. A. 98, 6859–6864.

Mishra, A., Reynolds, J.P., Chen, Y., Gourine, A.V., Rusakov, D.A., Attwell, D., 2016. Astrocytes mediate neurovascular signaling to capillary pericytes but not to arterioles. Nat. Neurosci. 19, 1619–1627.

Mutsaerts, H.J., Steketee, R.M., Heijtel, D.F., Kuijer, J.P., van Osch, M.J., Majoie, C.B., Smits, M., Nederveen, A.J., 2014. Inter-vendor reproducibility of pseudo-continuous arterial spin labeling at 3 Tesla. PloS One 9 e104108.

Nielsen, T.H., Olsen, N.V., Toft, P., Nordstrom, C.H., 2013. Cerebral energy metabolism during mitochondrial dysfunction induced by cyanide in piglets. Acta Anaesthesiol. Scand. 57, 793–801.

Okell, T.W., Chappell, M.A., Kelly, M.E., Jezzard, P., 2013. Cerebral blood flow quantification using vessel-encoded arterial spin labeling. J. Cerebr. Blood Flow Metabol. 33, 1716–1724.

Pilkinton, D.T., Hiraki, T., Detre, J.A., Greenberg, J.H., Reddy, R., 2012. Absolute cerebral blood flow quantification with pulsed arterial spin labeling during hyperoxia corrected with the simultaneous measurement of the longitudinal relaxation time of arterial blood. Magn. Reson. Med. 67, 1556–1565.

Powers, W.J., Videen, T.O., Markham, J., Black, K.J., Golchin, N., Perlmutter, J.S., 2008. Cerebral mitochondrial metabolism in early Parkinson's disease. J. Cerebr. Blood Flow Metabol. 28, 1754–1760.

Schmithorst, V.J., Hernandez-Garcia, L., Vannest, J., Rajagopal, A., Lee, G., Holland, S.K., 2014. Optimized simultaneous ASL and BOLD functional imaging of the whole brain. J. Magn. Reson. Imag. 39, 1104–1117.

Sette, G., Baron, J.C., Mazoyer, B., Levasseur, M., Pappata, S., Crouzel, C., 1989. Local brain haemodynamics and oxygen metabolism in cerebrovascular disease. Positron emission tomography. Brain 112 (Pt 4), 931–951.

Severinghaus, J.W., 1979. Simple, accurate equations for human blood O2 dissociation computations. J. Appl. Physiol. Respir. Environ. Exerc. Physiol. 46, 599–602.

Shin, D.D., Liu, H.-L., Wong, E.C., Liu, T.T., 2011. Effect of background suppression on CBF quantitation in pseudo continuous arterial spin labeling. Proc. Intl. Soc. Mag. Reson. Med. 19.

Smith, S., Brady, M., 1997. SUSAN - a new approach to low level image processing. Int. J. Comput. Vis. 23, 45–78.

Stefanovic, B., Hutchinson, E., Yakovleva, V., Schram, V., Russell, J.T., Belluscio, L., Koretsky, A.P., Silva, A.C., 2008. Functional reactivity of cerebral capillaries. J. Cerebr. Blood Flow Metabol. 28, 961–972.

Vafaee, M.S., Gjedde, A., 2000. Model of blood-brain transfer of oxygen explains nonlinear flow-metabolism coupling during stimulation of visual cortex. J. Cerebr. Blood Flow Metabol. 20, 747–754.

Vafaee, M.S., Vang, K., Bergersen, L.H., Gjedde, A., 2012. Oxygen consumption and blood flow coupling in human motor cortex during intense finger tapping: implication for a role of lactate. J. Cerebr. Blood Flow Metabol. 32, 1859–1868.

Valabregue, R., Aubert, A., Burger, J., Bittoun, J., Costalat, R., 2003. Relation between cerebral blood flow and metabolism explained by a model of oxygen exchange. J. Cerebr. Blood Flow Metabol. 23, 536–545.

Wang, X., Wang, W., Li, L., Perry, G., Lee, H.G., Zhu, X., 2014. Oxidative stress and mitochondrial dysfunction in Alzheimer's disease. Biochim. Biophys. Acta 1842, 1240–1247.

Winkler, E.A., Sengillo, J.D., Sullivan, J.S., Henkel, J.S., Appel, S.H., Zlokovic, B.V., 2013. Blood-spinal cord barrier breakdown and pericyte reductions in amyotrophic lateral sclerosis. Acta Neuropathol. 125, 111–120.

Wise, R.G., Harris, A.D., Stone, A.J., Murphy, K., 2013. Measurement of OEF and absolute CMRO2: MRI-based methods using interleaved and combined hypercapnia and hyperoxia. Neuroimage 83, 135–147.

Yemisci, M., Gursoy-Ozdemir, Y., Vural, A., Can, A., Topalkara, K., Dalkara, T., 2009. Pericyte contraction induced by oxidative-nitrative stress impairs capillary reflow despite successful opening of an occluded cerebral artery. Nat. Med. 15, 1031–1037.

Zhang, Y., Brady, M., Smith, S., 2001. Segmentation of brain MR images through a hidden Markov random field model and the expectation-maximization algorithm. IEEE Trans. Med. Imag. 20, 45–57.

Zheng, Y., Martindale, J., Johnston, D., Jones, M., Berwick, J., Mayhew, J., 2002. A model of the hemodynamic response and oxygen delivery to brain. Neuroimage 16, 617–637.

Zlokovic, B.V., 2011. Neurovascular pathways to neurodegeneration in Alzheimer's disease and other disorders. Nat. Rev. Neurosci. 12, 723–738.